

Influence of Modeling Choices on Nonlinear-Dynamic Behavior of a Single-Layer Reticulated Dome

Akshay Arun SOMKUWAR
Candidate for the Degree of Doctor of Engineering
Supervisor: Associate Professor Dr. Ryota Matsui
Division of Architectural and Structural Design

1. Introduction

In the numerical simulation of inelastic systems, the inertia forces generally retain their initial conditions, while the parameters governing restoring and damping forces must be adjusted based on modeling choices for the elastic-plastic behavior to ensure consistent simulated responses. In steel structures, inappropriate parameter selection can lead to inconsistencies, particularly when individual members¹⁾ experience rapid stiffness changes due to instabilities such as global buckling. Furthermore, under large, repeated earthquake excitations, structural members may experience local buckling, resulting in sudden degradation in both strength and stiffness.

Fiber elements are commonly used in simulating restoring force, as they reliably track the propagation of plasticity and effectively reproduce such instabilities. However, the accuracy of computational results for highly nonlinear behaviors depends heavily on discretization schemes and element formulations. Experimental vibration tests have shown that the damping ratios in structures remain relatively constant across relevant vibration modes²⁾. However, since the frequencies of inelastic systems differ from those of elastic systems, damping models based on initial stiffness can introduce unintended spurious damping forces³⁾.

This study examines the impact of modeling choices on the response of steel structures, with particular emphasis on element formulations, damping models, and the calibration of material models to accurately capture degradation mechanism associated with instabilities.

2. Validation of axially-loaded members

Axial force predominantly governs the behavior of individual members in spatial structures, such as steel reticulated domes, with their response closely resembling that of steel braces in multi-story braced frames. Building on the methodology proposed in the past study⁴⁾ regarding steel braces, this section investigates the force-deformation relationship of axially-loaded members in a reticulated dome. This focus is particularly relevant as the dome comprises members with varying slenderness ratios that have not fully validated.

Segmented beam-column models using force- and displacement-based formulation with fiber discretization, were selected to account for the inelastic interaction between axial force and flexural moment in axially-loaded members. These models are based on the Euler Bernoulli theory, which assumes that plane sections remain before and after the deformation. This modeling approach is commonly referred to as the fiber element. Fig. 1 illustrates the numerical scheme of the fiber element. For the comparative study between simulated and tested responses, the axially-loaded members commonly assigned in the reticulated dome as described in the following section, were subdivided into 2, 4, 8, 10, and 30 segments. An initial camber displacement at the midpoint of

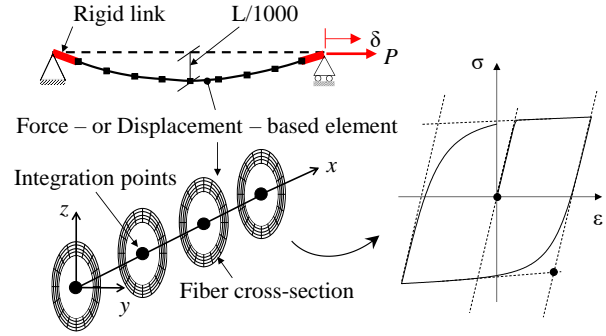


Fig. 1 Numerical scheme of beam – column element

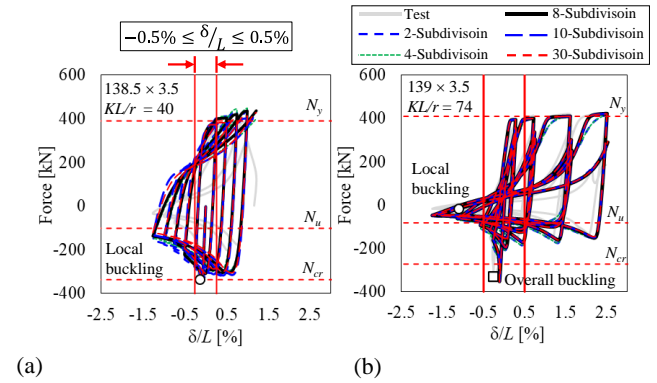


Fig. 2 Force – Deformation response for displacement-based fiber element (a) $KL/r = 40$; (b) $KL/r = 74$

the axially-loaded member was set to 0.1% of the total length as suggested by the past study⁴⁾. The cross section was discretized into 16 circumferential and 4 radial fibers. The material parameters were utilized from past studies⁴⁾. The Giuffré-Menegotto-Pinto model, implemented as Steel 02 in OpenSees, was used for the hysteretic response of material incorporating both kinematic and isotropic hardening. Fig. 2 presents the comparison of simulated and tested response. Since both formulations produced similar results, only the response from the displacement-based formulation was shown. All subdivision cases successfully captured the peak compressive strength of the axially-loaded members within an error margin of less than 6%. For a steel brace in which overall buckling ($KL/r = 74$) occurred before local buckling, the numerical model accurately captured the post-buckling stiffness. However, for a steel brace ($KL/r = 40$) in which local buckling occurred before or simultaneously with overall buckling, the numerical model predicted a stiffer post buckling response. The simulated response closely matched the tested response within the normalized deformation range of $\delta/L = -0.5\%$ to 0.5% , where δ is the deformation and L is the total length of steel brace.

3. Numerical model of Dome

This section outlines the scheme for the time history analysis of the reticulated dome. As illustrated in Fig. 3, the dome was pin-connected to the ground at all supports. A roof load of 1.80 kN/m² was applied as concentrated vertical nodal loads at the joints. Masses at all nodes were computed by a 3D structural analysis and design software STAAD. Nodal mass which equals nodal weight divided by gravitational acceleration, was introduced in all six degrees of freedom. The dimensions of the members in the reticulated dome were selected to ensure that all the members remained elastic under this roof load. The dome was constructed from round-hollow-steel-section members with a diameter 120 mm and a thickness 4.5 mm, which were rigidly connected to each other. The slenderness ratio of the members, taking the joint-to-joint distance as their length, ranged from 30 to 62. Yield strength σ_y of 235 MPa and kinematic hardening of 0.01 times elastic modulus were derived from Yang et al.⁵⁾. The elastic modulus was defined as 205 GPa. An initial camber of 0.003 times the total length, modelled as a half sine wave, was assigned for the members, which met the technical recommendations provided by AIJ. The natural period of the dome was 0.31 s at mode 1. The dome was designed to ensure stability under the dead load, and sustain insignificant and moderate damage states when subjected to Taft ground motions at Station 111 in the EW direction, with peak accelerations scaled to 0.45 g and 0.7 g, respectively, based on conventional design⁶⁾.

The fiber elements and material properties described in the preceding sections were adopted. The axial members were subdivided into 2, 4, 8, or 10 fiber elements, using either force-based or displacement-based formulation. The discretization scheme for the elements remained consistent. The Newmark's method was used with parameters $\gamma = 0.5$ and $\beta = 0.25$. The time increment of 0.001 s was selected based on a convergence study. The following three damping models were employed: Model 5, $[c] = a_0[m] + a_1[k]$; Model 6, $[c] = a_0[m] + a_1[k^*]$; and Model 12, $[c] = [m][\beta_0][m]$, the naming convention was followed as per Fukutomi et al.⁷⁾. In these equations: β_0 is the modal matrix defined by Eq. (1) and proposed by Wilson and Penzien⁸⁾; a_0 and a_1 are the coefficients for damping matrix.

$$[\beta_0] = \frac{2\zeta_n \omega_n \{\Phi_n\} \{\Phi_n\}^T}{M_n} \quad (1)$$

In the above equation, ω_n is the frequency of mode n , M_n is the modal mass of mode n . Damping ratio of 0.02 was set in modes 1 and 120 for Damping Models 5 and 6. For Damping Model 12, damping ratio of 0.02 was used in first 200 modes.

For Case A, the same ground motion used by Yang et al.⁵⁾ was adopted, with the Taft ground motions scaled to achieve peak ground acceleration (PGA) of 0.5g and 0.7 g. The former motion was applied to elastic analysis, this was conducted using a higher yield strength of 700 MPa for the material property to avoid any tension yielding of the fibers.

The latter motion, approximately 1.3 times the design spectrum of the Japanese Building Standard at safety limit for soil type 2, shown in Fig. 4, was used for elastic-plastic system. For Case B, a suite of ground motions for the near-field set including fault-normal and fault parallel was selected

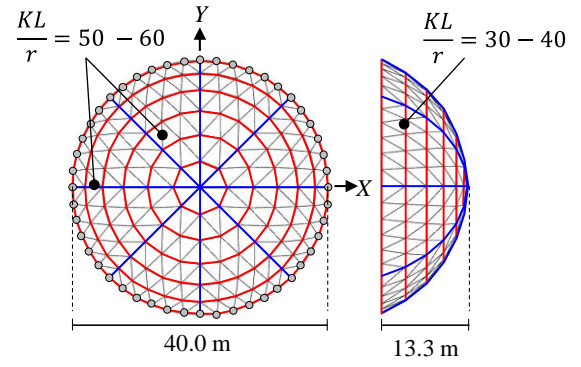


Fig. 3 Schematic of spherical dome

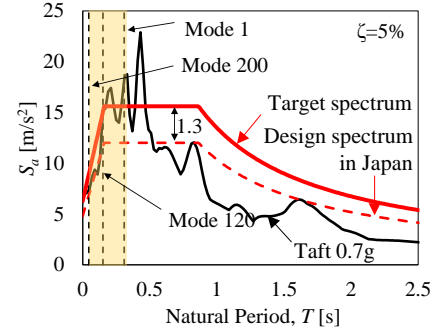


Fig. 4 Response spectrum of input ground motion

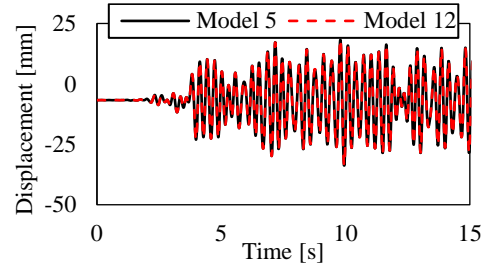


Fig. 5 Peak vertical elastic displacement response

based on FEMA P695⁹⁾. All ground motions were applied in the x -direction.

4. Response of Dome subjected to Taft ground motion – Case A

Fig. 5 shows peak vertical displacement for force-based model, the simulated elastic displacement histories from OpenSees with 8 elements were identical between Damping Models 5 and 12 and between both the formulations. It is noted that Models 5 and 6 are identical during elastic response.

To introduce a universal index for examining the influence of damping models on damping ratios in inelastic systems, Fukutomi et al.⁷⁾ suggested a representative damping ratio ζ_{rep} calculated as per Eq. 2-5.

$$\zeta_{n,eq} = \frac{\{\Phi_n^*\}^T [c] \{\Phi_n^*\}}{2 \cdot \omega_n^* \cdot \{\Phi_n^*\}^T [m] \{\Phi_n^*\}} \quad (2)$$

$$\gamma_n^* = \frac{M_n^*}{\sum_{n=1}^N M_n} \quad (3)$$

$$M_n^* = (\Gamma_n^*)^2 \cdot M_n \quad (4)$$

$$\zeta_{rep} = \sum_{n=1}^N \zeta_{n,eq} \cdot \gamma_n^* \quad (5)$$

In the above equations, ω_n^* is the frequency of elastic-plastic system updated step by step, γ_n^* is the ratio of effective modal mass to total mass, M_n^* is the effective modal mass, and Γ_n is the modal participation factor, and $N=200$ is the number of modes considered in the analysis. Fig. 6 presents the equivalent damping ratio $\zeta_{n,eq}$ at 15 seconds, as an example of plastic system using the displacement-based fiber element with 8 segments. For Damping Model 5, the equivalent damping ratios of plastic system deviate from those of elastic system, ranging from -5.5% to 30% across the corresponding modes. This discrepancy arose from damping Model 5's inability to maintain proportionality in the elastic-plastic system. Conversely, for Damping Model 6, although the equivalent damping ratio aligned with the initial-stiffness-proportional Rayleigh curve used in Damping Model 5 of elastic system, different damping ratios were observed for updated frequencies due to the decrease in frequencies compared to elastic system. In plastic system, Damping Model 5 exhibited equivalent damping ratios that were 0.94 to 1.46 times higher than those of Damping Model 6. For Damping Model 12, the equivalent damping ratio retained at the initial value of 0.02 up to mode 460, where the cumulative mass participation reached 99%.

Fig. 6 also illustrate the change in frequency of the reticulated dome for modes 1 and 120 in blue dashed line for Damping model 6. A general tendency of decrease in frequency over the time was observed for all three Damping models in both element formulations. Damping Model 5 exhibited the smallest decrease in frequency compared to Damping Models 6 and 12, due to its higher representative damping ratio. This tendency corresponds to the result of a shake table test for a scaled dome model by Nanhai et al.¹⁰⁾ that observed a decrease in fundamental frequency with increasing PGA, indicating a gradual reduction in structural stiffness. However, in the simulated results no significant effect on higher modes was observed. Mode 1 was the dominant mode in the horizontal x -direction, based on mass participation ratio. These results suggest that damping models and element formulation have impact on the dynamic response of the dominant mode, which plays a more substantial role in the global structural response.

Fig. 7 illustrates the representative damping ratio for both formulations in all three directions over the 1 second between 15 and 16 seconds. This corresponds to the duration when the maximum displacement at a node was observed for Damping Model 12 with the displacement-based fiber element. For both formulations, the representative damping ratio of the inelastic system in Damping Model 5 was the largest among all damping models in all three directions. The mean representative damping ratios for all three directions in Damping Model 5 were 1.37 times the target value of 0.02 for the force-based formulation and 1.26 times the target value for the displacement-based formulation. In contrast, the mean representative damping ratios in all three directions for Damping Models 6 and 12 were 1.08 times and 0.95 times the target value of 0.02, respectively, for both formulations.

Fig. 8 shows the relative z -displacement (vertical) histories of a node at the apex. Since the simulated displacement distribution for the selected damping models were similar for both formulation at this node, only the results

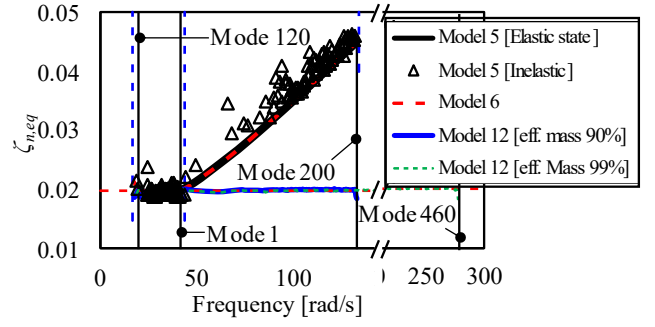


Fig. 6 Frequency vs. equivalent damping ratio for various damping models for inelastic system

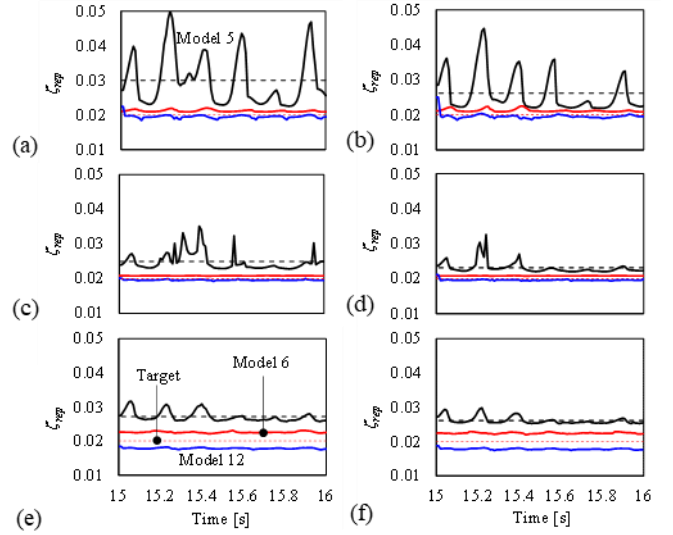


Fig. 7 Simulated representative damping ratio for force-based fiber element (a) x -dir.; (c) y -dir.; (e) z -dir.; for displacement-based fiber element (b) x -dir.; (d) y -dir.; (f) z -dir

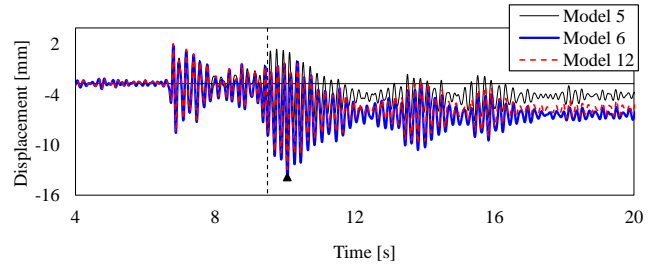


Fig. 8 Simulated relative vertical displacement histories for various damping model for force-based fiber element

for the force-based formulation are presented. Although the simulated residual displacement observed after 9.5 seconds was underestimated by Damping Model 5 at this node.

Fig. 9 illustrates the contour of vertical displacement at the instant when the maximum displacement was observed at a specific node. It is noteworthy that the timing of this maximum displacement varied depending on the damping model and the type of element formulation used. The displacement was concentrated at the nodes located in Ring No. 2, which corresponds to the circumferential members, as depicted in Fig. 9. For the force-based fiber element, Damping Models 5 and 12 exhibited symmetrical distributions of vertical deformations about the EW direction, with a peak displacement of approximately 55 mm, while Damping Model 6 demonstrated a higher peak displacement, close to

115 mm, along with negative displacements concentrated in the central zone. For the displacement-based fiber element, Damping Model 5 showed the lowest peak displacement, around 55 mm, accompanied by asymmetry along the NS direction. Meanwhile, Damping Models 6 and 12 displayed peak displacements of approximately 115 mm, with Damping Model 6 also exhibiting central negative displacement.

Although Damping Model 12 exhibited minimal sensitivity to element formulation in terms of deformation distribution patterns, the difference in peak displacement between the force-based and displacement-based formulations was significant. This discrepancy highlights the importance of carefully evaluating the choice of element formulation when analyzing peak responses. While the deformation contours remain relatively consistent, the marked difference in peak values can significantly impact overall structural performance predictions, particularly under critical loading conditions.

5. Response of Dome subjected to Taft ground motion – Case B

This section describes the nonlinear response of reticulated dome subjected to the suite of 28 pairs of ground motions selected by FEMA-P-695⁹⁾.

Fig. 10 shows the maximum displacement response for Case B, for representative nodes and for each damping model. The lognormal distribution was used to compute median and 84th percentile displacement as a representative response of the reticulated dome subjected to the suite of ground motions, for the maximum displacement experienced. Damping Model 5, i.e., initial-stiffness-proportional Rayleigh Damping, exhibited the smallest displacement response in most cases. This may be due to the spurious damping force resulting in reduced displacement. Damping Model 6, tangent-stiffness-proportional Rayleigh Damping frequently showed the largest displacement response. Since Damping Model 12, which represents modal damping, was considered the most realistic among these damping models based on the measurement of damping ratios, Damping Model 6 may be overly conservative. For fault-normal ground motion, the seismic risk as dictated by the study¹¹⁾, associated with Record Serial Number 1529 listed in Table A-6C in FEMA-P-695⁹⁾, was found to be lower when analyzed using Damping Model 5 compared to Damping Models 6 and 12. A similar trend was observed in several other cases.

Fig. 11 illustrates the elongation of all axially-loaded members and the ratio of the number of members experiencing more than 0.5% contraction to the total number of all members, for each case of the reticulated dome subjected to the fault normal ground motions. At least 95% of

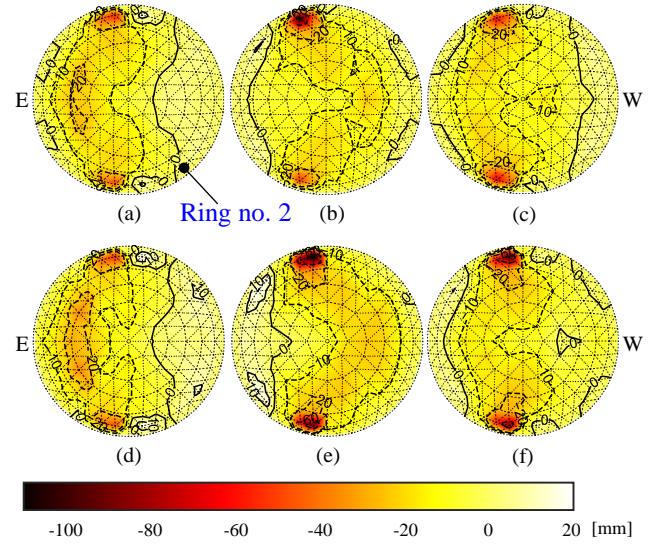


Fig. 9 The contour of vertical displacement at the instance of peak response for force-based fiber element (a) Damping Model 5; (b) Model 6; (c) Model 12; for displacement-based fiber element (d) Model 5; (e) Model 6; (f) Model 12

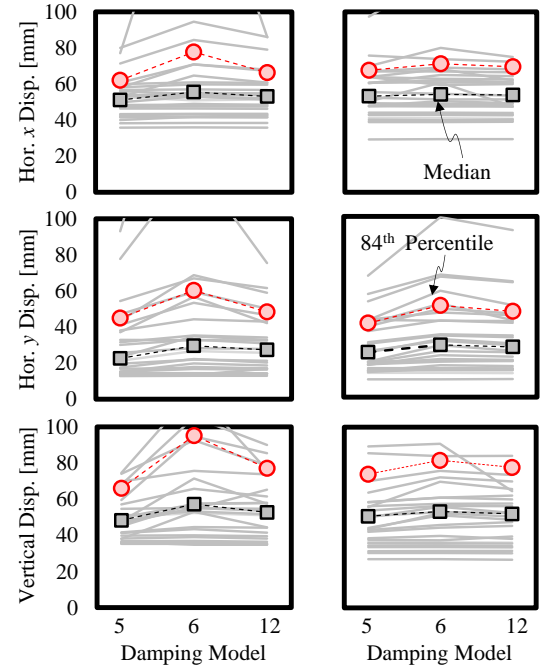


Fig. 10 Maximum displacement of reticulated dome subjected to fault normal (a) x-dir.; (b) y-dir.; (c) vertical dir.; fault parallel (d) x-dir.; (e) y-dir.; (f) vertical dir.

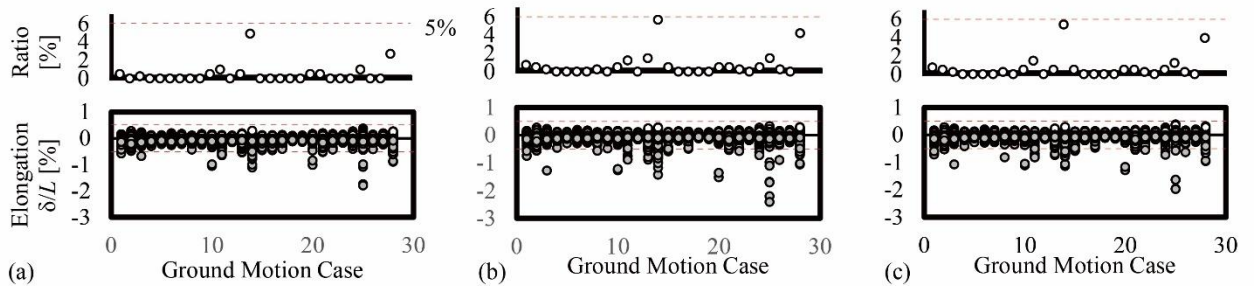


Fig. 11 Ratio of the number of members experienced contraction more than 5% to that of the total members, maximum elongation and contraction of the members subjected to the fault normal ground motion: (a) Damping model 5; (b) Model 6; (c) Model 12

the members, deformation in the range -0.5% to 0.5%. The validated axially loaded members showed excellent agreement within this range.

6. Modelling of local buckling induced degradation

Suzuki and Lignos (2020) introduced a material model (SL Model) based on the Unified Voce-Chaboche (UVC) uniaxial material model, incorporating both isotropic and kinematic hardening to capture degradation in HSS columns. The model was later extended to account for local buckling-induced degradation in round HSS.

The parameters for the SL Model were calibrated using HSS stub columns with diameter-to-thickness ratios ranging from 19 to 57. To eliminate variability in the stress-strain curve during calibration, the yield ratio was selected between 1.0 and 1.3. The yield strength ranged between 357 and 454 MPa. The SL Model was further refined for round HSS braces with effective slenderness ratios KL/r ranging from 16 to 103 through comprehensive cyclic parameter adjustments were made to ensure reliable simulation results. Fig. 12 presents the effective stress-strain relationship developed by Suzuki and Lignos (2020) to capture compression degradation caused by local buckling. The cyclic behavior depends on the diameter-to-thickness ratio D/t , with the material parameter defining the cyclic curve following a power law, as given in Eq. 6.

$$CP = a \left(\frac{D}{t} \times \frac{\sigma_{y,m}}{E} \right)^b \quad (6)$$

Where, CP refers to parameter of interest, either $\sigma_{c,m}/\sigma_{y,m}$, $\epsilon_{c,m}/\epsilon_{y,m}$, $E_{d1,m}/E$, $\sigma_{d,m}/\sigma_{c,m}$, and a and b are empirical parameters calibrated by regression coefficients based on a specific suite of stud column data. $E_{d2,m}/E$ was set to -0.005.

Fig. 13 compares the loading curve from calibration model and the selected stud columns used to calibrate the parameters that define softening branch in compression, the parameters are chosen to match strain hardening to maximum strength and degradation slope over the range of the D/t ratio. The range of the D/t ratios was between 19 and 57, thereby covering stocky to slender range. The predicted equation is able to capture the post-buckling behavior with sufficient accuracy.

Table 1 provides the calibrated equation for defining material properties under monotonic loading. In the post-buckling phase, the second negative stiffness modulus was set to 0.5% of the elastic modulus. The accuracy of the equations can be improved by expanding the dataset for stub columns with round HSSs or by performing virtual stud column tests using finite element software to address the gaps in the data.

Fig. 14 compares hysteresis response from the SL Model that closely aligns with the experimental data, demonstrating improved accuracy in capturing post-buckling behavior. In the experimental test, local distortion initiated during the 16th loading cycle. In the simulation the local buckling was delayed until the 14th loading cycle indicated by the red line, after which the force deformation continued along the black line, significantly improving the accuracy in replicating the post-buckling behavior observed in the test.

The calibrated SL model is being implemented in the 8-story chevron braced frame designed as per US provision¹⁴, with lateral loads primarily resisted by the chevron braces and

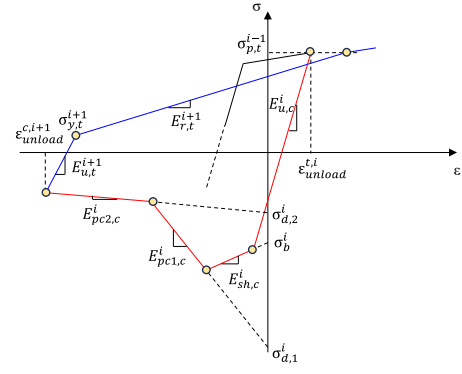


Fig. 12 Effective stress – strain material parameters¹¹⁾

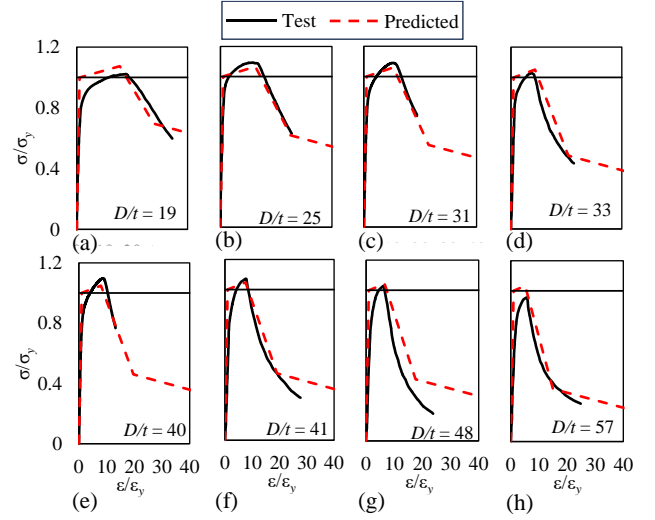


Fig. 13 Normalized stress – strain curve for selected stub column test¹³⁾

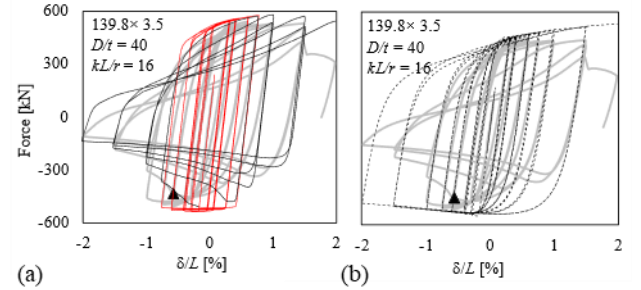


Fig. 14 Comparison of load-deformation for brace: (a) SL Model; and (b) Steel02.

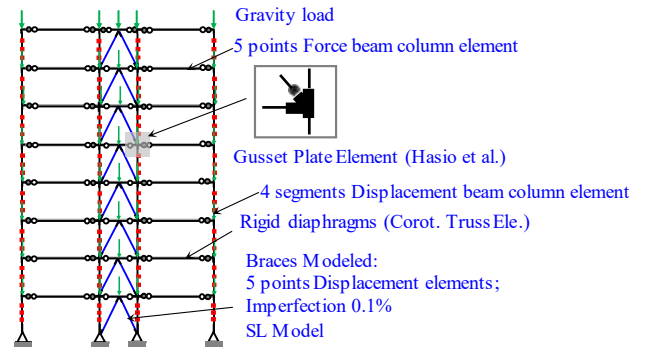


Fig. 15 Numerical scheme for 8 story chevron braced frame

simply supported beam to remain elastic, the numerical scheme is illustrated in Fig. 15. A pushover analysis of the

braced frame model was conducted to evaluate performance. Lateral loads were incrementally applied up to a target roof drift of 0.04 radians. The results showed story drifts concentrated in the bottom three stories with the Steel02 material and the bottom four with the SL model, while the upper stories remained predominantly elastic, as shown in Fig. 16. Sudden drops in base shear on higher floors suggest instability, in case of SL Model requiring further investigation and calibration.

Conclusion

This study examined numerical modeling choices for element formulations and damping models in the dynamic response of steel structures. A spherical reticulated dome with a 40-m span and 13-m height was used to evaluate the seismic performance of spatial structures under various ground motions. A deteriorating material model was integrated into OpenSees to replicate local buckling-induced degradation in steel braces, and this approach was applied to assess the lateral resistance of a chevron-braced frame. The main findings are as follows:

1. The choice of modeling parameters, such as force formulations and damping models, had minimal influence on the elastic response of the reticulated dome. However, these choices significantly affected the elastic-plastic response, despite the limited plasticity of the system. This finding for spatial structures differs from Chopra et al. study¹⁵, which suggested that damping models had limited impact on dynamic responses of multi-story frames with the distributed plasticity models.
2. The average damping ratios for Damping Model 5 in all three directions were 1.26 times the target, while Models 6 and 12 produced ratios nearly identical to the target. Displacement responses using Model 6 were 1.1 to 1.2 times higher than those with Model 12 across the ground motions analyzed. Consequently, Model 12 emerged as the most reliable choice for spatial structures.
3. Damping Model 5 was found to potentially yield a more unconservative evaluation of damage state for spatial structures than Models 6 and 12. Damping Model 12 is recommended for the seismic risk analysis to mitigate the effects of the spurious damping forces.
4. The SL Model successfully captured the force–deformation behavior of round-HSS braces by calibrating material parameters derived from stub column tests. While numerical instabilities were observed when the SL Model was applied in the static pushover analysis, it effectively reproduced the degradation of the lateral resistance in the chevron braced frame caused by local buckling.

References

- 1) Guide to Earthquake Response Evaluation of Metal Roof Spatial Structures. Proceedings of IASS Annual Symposia, IASS 2015 Amsterdam Symposium: Future Visions – Metal Spatial Structures, pp. 1-12(12).
- 2) Tatemichi, Ikuo, Tatsuo Hatato, Yoshimichi Anma, and Satoshi Fujiwara. 1997. “Vibration Tests on a Full-Size Suspen-Dome Structure.” *International Journal of Space Structures* 12 (3–4): 217–24. <https://doi.org/10.1177/026635119701200310>.
- 3) Charney, Finley A. 2008. “Unintended Consequences of Modeling Damping in Structures.” *Journal of Structural Engineering* 134 (4): 581–92. [https://doi.org/10.1061/\(ASCE\)0733-9445\(2008\)134:4\(581\)](https://doi.org/10.1061/(ASCE)0733-9445(2008)134:4(581)).
- 4) P. Uriz, F.C. Filippou, S.A. Mahin, Model for cyclic inelastic buckling of steel braces, *J. Struct. Eng.* 134 (2008) 619–628, [https://doi.org/10.1061/\(asce\)0733-9445\(2008\)134:4\(619\)](https://doi.org/10.1061/(asce)0733-9445(2008)134:4(619)).
- 5) F. Yang et al. Effect of complex damping on seismic responses of a reticulated dome and shaking table test validation. *Thin-Walled Structures* 134, 407–418, 2019.
- 6) Zhi, X. D., G. B. Nie, F. Fan, and S. Z. Shen. 2012. “Vulnerability and Risk Assessment of Single-Layer Reticulated Domes Subjected to Earthquakes.” *Journal of Structural Engineering* 138 (12): 1505–14. [https://doi.org/10.1061/\(asce\)st.1943-541x.0000589](https://doi.org/10.1061/(asce)st.1943-541x.0000589).
- 7) S. Fukutomi, T. Okazaki, R. Matsui, T. Asari, Influence of viscous damping model on time-history response analysis of elastic-plastic systems (Part I): comparison of damping models, *J. Struct. Constr. Eng.* 85 (2020) 1555–1563, <https://doi.org/10.3130/AIJS.85.1555>.
- 8) E.L. Wilson, J. Penzien, Evaluation of orthogonal damping matrices, *Int. J. Numer. Methods Eng.* 4 (1972) 5–10, <https://doi.org/10.1002/nme.1620040103>.
- 9) FEMA P695, Quantification of Building Seismic Performance Factors, FEMA P695, 2009, pp. 1–421.
- 10) Z. Nanhai, Y. Jihong, Structural vulnerability of a single-layer dome based on its form, *J. Eng. Mech.* 140 (2014) 112–127, [https://doi.org/10.1061/\(asce\)em.1943-7889.0000636](https://doi.org/10.1061/(asce)em.1943-7889.0000636).
- 11) G.N. Nie, C. xiao Zhang, X. dong Zhi, J. Dai, Damage quantification, damage limit state criteria and vulnerability analysis for single-layer reticulated shell, *Thin-Walled Struct.* 120 (2017) 378–385. <https://doi.org/10.1016/j.tws.2017.09.007>.
- 12) Suzuki, Yusuke, and Dimitrios G. Lignos. 2020. “Fiber-Based Hysteretic Model for Simulating Strength and Stiffness Deterioration of Steel Hollow Structural Section Columns under Cyclic Loading.” *Earthquake Engineering and Structural Dynamics* 49 (15): 1702–20. <https://doi.org/10.1002/eqe.3324>.
- 13) Elchalakani, Mohamed, Xiao-Ling Zhao, and Raphael Grzebieta. 2002. “Tests on Concrete Filled Double-Skin (CHS Outer and SHS Inner) Composite Short Columns under Axial Compression.” *Thin-Walled Structures* 40 (5): 415–41. [https://doi.org/10.1016/S0263-8231\(02\)00009-5](https://doi.org/10.1016/S0263-8231(02)00009-5).
- 14) Dias, Ilanildo. 2023. “Seismic Performance and Design of Japanese Steel Chevron Braced Moment Resisting Frames.” Hokkaido University. Hokkaido University.
- 15) Chopra, A. K., and F. McKenna. 2016. “Modeling Viscous Damping in Nonlinear Response History Analysis of Buildings for Earthquake Excitation.” *Earthquake Engineering and Structural Dynamics* 45 (2): 193–211. <https://doi.org/10.1002/eqe.2622>.

Table 1 Calibrated monotonic parameters for round HSS

Parameter	σ_c/σ_y	$\varepsilon_c/\varepsilon_y$	E_{d1}/E	σ_d/σ_c	E_{d2}
a	0.92	0.37	-0.34	0.061	-0.005E
b	-0.052	-1.17	0.74	-0.742	

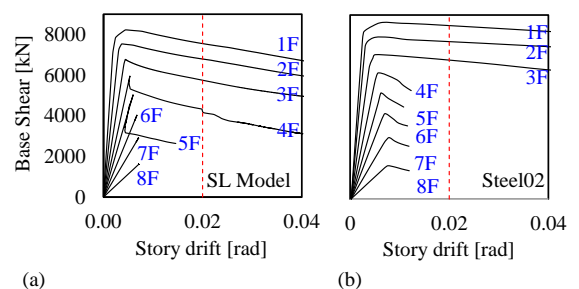


Fig. 16 Comparison of push over curve for 8 story steel chevron frames between SL Model and Steel02